The Astrophysical Journal, 798:39 (12pp), 2015 January 1 doi:10.1088/0004-637X/798/1/39
© 2015. The American Astronomical Society. All rights reserved.

EARLY OBSERVATIONS AND ANALYSIS OF THE TYPE Ia SN 2014J IN M82

G. H. Marion[1], D. J. Sand[2], E. Y. Hsiao[3,4], D. P. K. Banerjee[5], S. Valenti[6,7], M. D. Stritzinger[4], J. Vinkó[1,8], V. Joshi[5], V. Venkataraman[5], N. M. Ashok[5], R. Amanullah[9], R. P. Binzel[10], J. J. Bochanski[11], G. L. Bryngelson[12], C. R. Burns[13], D. Drozdov[14], S. K. Fieber-Beyer[15], M. L. Graham[16], D. A. Howell[6,7], J. Johansson[9], R. P. Kirshner[17], P. A. Milne[18], J. Parrent[17], J. M. Silverman[1], R. J. Vervack, Jr.[19], and J. C. Wheeler[1]
[1] University of Texas at Austin, 1 University Station C1400, Austin, TX 78712-0259, USA; hman@astro.as.utexas.edu
[2] Physics Department, Texas Tech University, Lubbock, TX 79409, USA
[3] Carnegie Observatories, Las Campanas Observatory, Colina El Pino, Casilla 601, Chile
[4] Department of Physics and Astronomy, Aarhus University, Ny Munkegade 120, DK-8000 Aarhus C, Denmark
[5] Astronomy and Astrophysics Division, Physical Research Laboratory, Navrangapura, Ahmedabad - 380009, Gujarat, India
[6] Las Cumbres Observatory Global Telescope Network, 6740 Cortona Drive, Suite 102, Santa Barbara, CA 93117, USA
[7] Department of Physics, Broida Hall, University of California, Santa Barbara, CA 93106, USA
[8] Department of Optics and Quantum Electronics, University of Szeged, Domter 9, 6720 Szeged, Hungary
[9] The Oskar Klein Centre, Physics Department, Stockholm University, Albanova University Center, SE 106 91 Stockholm, Sweden
[10] Department of Earth, Atmospheric, and Planetary Sciences, Massachusetts Institute of Technology, Cambridge, MA 02139, USA
[11] Haverford College, 370 Lancaster Avenue, Haverford, PA 19041, USA
[12] Department of Physics and Astronomy, Francis Marion University, 4822 East Palmetto Street, Florence, SC 29506, USA
[13] Observatories of the Carnegie Institution for Science, 813 Santa Barbara Street, Pasadena, CA 91101, USA
[14] Department of Physics and Astronomy, Clemson University, 8304 University Station, Clemson, SC 29634, USA
[15] Department of Space Studies, University of North Dakota, University Stop 9008, ND 58202, USA
[16] Astronomy Department, University of California at Berkeley, Berkeley, CA 94720, USA
[17] Harvard-Smithsonian Center for Astrophysics, 60 Garden Street, Cambridge, MA 02138, USA
[18] University of Arizona, Steward Observatory, 933 North Cherry Avenue, Tucson, AZ 85719, USA
[19] The Johns Hopkins University Applied Physics Laboratory, Laurel, MD 20723, USA
Received 2014 May 15; accepted 2014 October 24; published 2014 December 18

ABSTRACT

We present optical and near infrared (NIR) observations of the nearby Type Ia SN 2014J. Seventeen optical and 23 NIR spectra were obtained from 10 days before (−10d) to 10 days after (+10d) the time of maximum *B*-band brightness. The relative strengths of absorption features and their patterns of development can be compared at one day intervals throughout most of this period. Carbon is not detected in the optical spectra, but we identify C I λ1.0693 in the NIR spectra. Mg II lines with high oscillator strengths have higher initial velocities than other Mg II lines. We show that the velocity differences can be explained by differences in optical depths due to oscillator strengths. The spectra of SN 2014J show that it is a normal SN Ia, but many parameters are near the boundaries between normal and high-velocity subclasses. The velocities for O I, Mg II, Si II, S II, Ca II, and Fe II suggest that SN 2014J has a layered structure with little or no mixing. That result is consistent with the delayed detonation explosion models. We also report photometric observations, obtained from −10d to +29d, in the *UBVRIJH* and K_s bands. The template fitting package SNooPy is used to interpret the light curves and to derive photometric parameters. Using $R_V = 1.46$, which is consistent with previous studies, SNooPy finds that $A_V = 1.80$ for $E(B-V)_{\rm host} = 1.23 \pm 0.06$ mag. The maximum *B*-band brightness of -19.19 ± 0.10 mag was reached on February 1.74 UT ± 0.13 days and the supernova has a decline parameter, Δm_{15}, of 1.12 ± 0.02 mag.

Key words: infrared: general – supernovae: general – supernovae: individual (2014J)

1. INTRODUCTION

Type Ia supernovae (SNe Ia) are of great importance both as standardizable candles and for their role in the chemical enrichment of the universe. SN Ia measurements have led to the discovery of the accelerated expansion of the universe (Riess et al. 1998; Perlmutter et al. 1999). Because of their importance and widespread use, it is very desirable to move beyond empirical relations to understand the evolution of the progenitor systems and the physics of the explosions.

One route to a deeper physical understanding of SNe Ia is through detailed study of very nearby events (see, e.g., Kirshner et al. 1973; Suntzeff et al. 1999; Jha et al. 1999; Nugent et al. 2011; Foley et al. 2012; Silverman et al. 2012; Childress et al. 2013; Zheng et al. 2013, among many others). When they are discovered soon after the explosion and closely monitored, nearby SNe can be observed from X-ray to radio wavelengths. The discovery of the Type Ia SN 2014J in M82, the closest SN Ia in a generation, offers a unique opportunity to study a supernova (SN) of this class in exquisite detail. These intensive observations lead to a more comprehensive view of the explosion and place strong constraints on the progenitor systems (see, for instance, the reviews of nearby SN 2011fe; Chomiuk 2013; Kasen 2013).

Near infrared (NIR) spectroscopy offers a unique perspective on nearby SNe Ia. The progenitors of SNe Ia are carbon–oxygen white dwarf stars, so the identification of carbon and mapping its distribution are key ingredients for constraining SNe Ia explosion models (Thomas et al. 2011a; Milne et al. 2013). The C I λ1.0693 line is strong and relatively isolated, making it a good indicator of material originating from the progenitor. Magnesium is a direct product of carbon burning, but not oxygen burning. Thus, observations of Mg II (with several strong lines in the NIR) measure the inner boundary of carbon burning, and help to define the regions of the progenitor that experienced a detonation-driven burning phase (Wheeler et al. 1998). The recent NIR spectroscopic analysis of SN 2011fe (Hsiao et al. 2013), and its accompanying meta-analysis of other

SNe Ia with NIR spectroscopy, emphasizes what time series NIR spectroscopy can accomplish. However, progress is limited because the current sample of SNe Ia with NIR spectroscopic time series is ∼100 times smaller than optical spectroscopic samples (see, e.g., Blondin et al. 2012; Yaron & Gal-Yam 2012; Boldt et al. 2014).

Several studies of SN 2014J have already reported the light curve (LC) rise, early spectroscopy, dust distribution along the line of sight, and possible progenitor systems (e.g., Zheng et al. 2014; Goobar et al. 2014; Nielsen et al. 2014; Kelly et al. 2014; Amanullah et al. 2014). Predictions have also been made for X-ray and gamma-ray LCs (The & Burrows 2014), along with initial detections of gamma ray lines (Churazov et al. 2014). Margutti et al. (2014) presented deep X-ray observations to probe the post-explosion environment of SN 2014J.

Here we investigate the spectroscopic properties of SN2014J from −10 days to +10 days relative to $t(B_{\max})$ with an emphasis on an exceptional sequence of NIR spectra taken at a near-daily cadence. This unique NIR sample, coupled with optical spectroscopy and the LC parameters, reveals the evolution of spectral features with a level of detail not previously seen in the NIR.

SN 2014J is located in M82, a nearby and vigorously star forming galaxy. The dusty environment produces a large extinction that affects both distance estimates to M82 and the inferred Milky Way extinction along the line of sight. Throughout this work, we adopt a distance modulus of $\mu = 27.64 \pm 0.1$ mag ($d = 3.4$ Mpc) to M82 based on the average of the two tip of the red giant branch distance measurements presented in Dalcanton et al. (2009), which are mildly in disagreement with each other. Visual inspection of Galactic dust maps (Schlegel et al. 1998; Schlafly & Finkbeiner 2011) shows clear contamination from M82 itself, biasing the Milky Way extinction contribution high. We thus take the approach of Dalcanton et al. (2009) and adopt a Milky Way extinction value based on regions surrounding M82, and use a $E(B-V)_{\rm MW} = 0.05$ mag when appropriate.

2. THE OBSERVATIONS

Here we present photometric and spectroscopic observations of SN 2014J. The highlight of this sample is the 23 NIR spectra of SN 2014J obtained during its rise to maximum and the ∼10 days following.

2.1. Optical and NIR Photometry

Optical photometry of SN 2014J was taken with a nearly daily cadence, utilizing the Las Cumbres Observatory Global Telescope Network's (LCOGT) facilities at the McDonald Observatory and the Faulkes Telescope North (Brown et al. 2013). Broadband data were collected in Johnson-Cousins *UBVRI* filters. These observations began on 2014 January 21 UT (−11d), which is ∼6 days after the first archival detections of the SN (Zheng et al. 2014), and they continued through March 3 (+29d). The LCOGT photometry is shown in Figure 1 and the observational details are given in Table 1.

All data were processed using a pipeline developed by the LCOGT SN team (e.g., Valenti et al. 2014), which employs standard image reduction procedures and point-spread function photometry in a python framework. Instrumental magnitudes are transformed to the standard Sloan Digital Sky Survey or Landolt filter system via standard star observations taken during photometric nights. We note that the SN 2014J LCOGT LC data

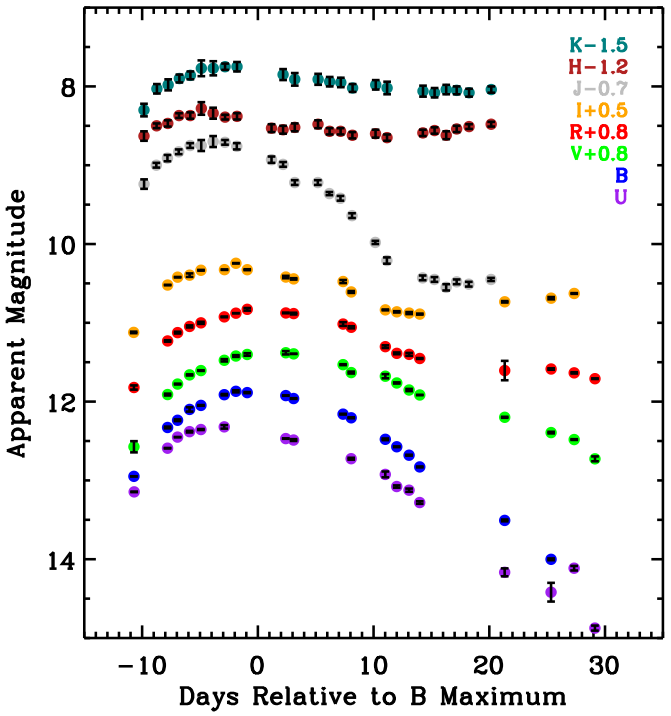

Figure 1. Photometry of SN 2014J from −11d to +29d. The observations were made at Mt. Abu (JHK_s) and by the LCOGT (*UBVRI*). The LC properties and the significant extinction of SN 2014J are discussed in Section 3. Photometric uncertainties are plotted, although there may be residual systematics due to M82 host galaxy contamination. Note that the NIR bands have not reached their secondary peaks at the final observation date in this sample.

through January 29 (−3d) have been published in Goobar et al. (2014), but the current work extends the coverage by more than 30 days. No Milky Way or M82 host galaxy extinction corrections have been applied to the photometry shown in Figure 1.

NIR photometry from the Mt. Abu Infrared Observatory (Banerjee & Ashok 2012) in the *JH* and K_s bands is also presented in Figure 1 and the observational details appear in Table 2. These observations began on January 22 (−10d) and they continued through February 22 (+20d) The NIR photometry through −3d has been presented by Goobar et al. (2014) and through +20d by Amanullah et al. (2014).

The Mt. Abu data were taken with the Near-Infrared Camera/Spectrograph (NICS), which has an 8 × 8 square arcmin field of view and was reduced in a standard way. Magnitudes were determined via aperture photometry, and are calibrated using Two Micron All Sky Survey (2MASS) stars in the field. Star J09553494+6938552, in the field of M82, was used as the primary photometric standard for calibration in the NIR bands. When possible, we cross-checked results with other 2MASS field stars, but J09553494+6938552 was always the primary standard.

2.2. Optical Spectroscopy

Optical spectroscopy of SN 2014J was obtained with the robotic FLOYDS spectrograph at FTN and the Andalucia Faint Object Spectrograph and Camera (ALFOSC) at the Nordic Optical Telescope (NOT) from January 23 (−9d) to February 10 (+9d). The FLOYDS data cover a wavelength range of ∼3200 to 10000 Å (via cross dispersion) and the ALFOSC spectra cover ∼3200 to 9100 Å (using grism 4 with 300 grooves per millimeter). All of the data were reduced in a standard manner

Table 1
Optical Photometry

MJD +56600	Phase wrt $t(B_{max})$	Mag Apparent	Err
	U band		
78.91	−10.9	13.15	0.003
81.80	−8.0	12.59	0.003
82.66	−7.1	12.45	0.002
83.70	−6.1	12.38	0.010
84.68	−5.1	12.35	0.006
86.70	−3.1	12.32	0.022
92.01	+2.2	12.47	0.002
92.69	+2.9	12.49	0.011
97.66	+7.9	12.72	0.012
100.61	+10.8	12.92	0.037
101.60	+11.8	13.08	0.014
102.67	+12.9	13.12	0.020
103.59	+13.8	13.28	0.016
110.93	+21.1	14.17	0.050
114.94	+25.1	14.42	0.119
116.93	+27.1	14.11	0.029
118.73	+28.9	14.87	0.032
	B band		
78.89	−10.9	12.95	0.001
81.80	−8.0	12.33	0.011
82.67	−7.1	12.24	0.011
83.70	−6.1	12.10	0.027
84.68	−5.1	12.05	0.005
86.70	−3.1	11.91	0.009
87.70	−2.1	11.87	0.013
88.68	−1.1	11.89	0.007
92.02	+2.2	11.92	0.003
92.69	+2.9	11.96	0.004
96.96	+7.2	12.16	0.005
97.67	+7.9	12.21	0.006
100.61	+10.8	12.48	0.011
101.60	+11.8	12.57	0.004
102.67	+12.9	12.68	0.006
103.59	+13.8	12.83	0.006
110.93	+21.1	13.51	0.011
114.94	+25.1	14.00	0.011
	V band		
78.89	−10.9	11.77	0.071
81.80	−8.0	11.11	0.012
82.67	−7.1	10.98	0.005
83.70	−6.1	10.86	0.007
84.68	−5.1	10.81	0.004
86.70	−3.1	10.68	0.015
87.70	−2.1	10.62	0.011
88.68	−1.1	10.60	0.016
92.02	+2.2	10.58	0.021
92.69	+2.9	10.59	0.002
96.96	+7.2	10.73	0.006
97.67	+7.9	10.83	0.012
100.62	+10.8	10.88	0.026
101.61	+11.8	10.96	0.007
102.67	+12.9	11.05	0.014
103.59	+13.8	11.12	0.001
110.93	+21.1	11.40	0.006
114.94	+25.1	11.59	0.010
116.94	+27.1	11.68	0.005
118.73	+28.9	11.93	0.031
	R band		
78.90	−10.9	11.02	0.027
81.81	−8.0	10.43	0.009
82.67	−7.1	10.32	0.011
83.70	−6.1	10.25	0.013
84.69	−5.1	10.20	0.013
86.70	−3.1	10.12	0.004
87.71	−2.1	10.08	0.001
88.68	−1.1	10.03	0.017
92.02	+2.2	10.07	0.004
92.69	+2.9	10.08	0.011
96.97	+7.2	10.22	0.024
97.67	+7.9	10.26	0.013
100.62	+10.8	10.50	0.017
101.61	+11.8	10.59	0.011
102.67	+12.9	10.60	0.018
103.59	+13.8	10.65	0.006
110.93	+21.1	10.81	0.123
114.94	+25.1	10.79	0.009
116.94	+27.1	10.84	0.008
118.73	+28.9	10.91	0.004
	I band		
78.87	−10.9	10.62	0.010
81.81	−8.0	10.02	0.003
82.67	−7.1	9.92	0.003
83.70	−6.1	9.90	0.022
84.69	−5.1	9.83	0.004
86.72	−3.1	9.83	0.003
87.71	−2.1	9.74	0.003
88.68	−1.1	9.83	0.006
92.02	+2.2	9.92	0.015
92.70	+2.9	9.94	0.009
96.97	+7.2	9.98	0.020
97.67	+7.9	10.11	0.012
100.62	+10.8	10.34	0.005
101.61	+11.8	10.36	0.008
102.67	+12.9	10.38	0.013
103.60	+13.8	10.39	0.007
110.93	+21.1	10.23	0.009
114.94	+25.1	10.19	0.015
116.94	+27.1	10.13	0.005

using IRAF routines. Optical spectra obtained before February 1 were previously published by Goobar et al. (2014). A log of the optical spectroscopy is presented in Table 3, and the data are plotted in Figure 2 alongside the NIR spectra.

2.3. Near-infrared Spectroscopy

NIR spectroscopy of SN 2014J was obtained with near-daily cadence utilizing the NASA Infrared Telescope Facility (IRTF) and the Mt. Abu Infrared Observatory from January 22 (−10d) to February 11 (+10d). All observations were taken using the classical ABBA technique, nodding the object along the slit, which was oriented along the parallactic angle. A log of the NIR spectroscopy is presented in Table 3, and the data are presented with the optical spectra in Figure 2.

Mt. Abu Infrared Observatory NIR spectra were taken with the 1.2 m telescope and its NICS, equipped with a 1024 × 1024 HgCdTe Hawaii array (Banerjee & Ashok 2012). Final spectra with wavelength coverage of 0.85–2.4 μm, at $R = 1000$ were obtained over three grating settings. Observations of an A-type star were used to correct for the effects of telluric atmospheric absorption. The data were reduced in a standard way using IRAF tasks, with a final flux calibration based on the broadband JHK_s

Table 2
Near Infrared Photometry

MJD +56600	Phase wrt $t(B_{max})$	Mag Apparent	Err
	J band		
79.77	−10.0	9.94	0.060
80.83	−9.0	9.70	0.030
81.79	−8.0	9.61	0.040
82.76	−7.0	9.53	0.030
83.75	−6.1	9.45	0.030
84.71	−5.1	9.45	0.070
85.74	−4.1	9.40	0.070
86.76	−3.0	9.41	0.030
87.78	−2.0	9.46	0.040
90.78	+1.0	9.63	0.040
91.78	+2.0	9.69	0.030
92.79	+3.0	9.92	0.030
94.78	+5.0	9.92	0.030
95.78	+6.0	10.06	0.020
96.74	+6.9	10.12	0.030
97.74	+7.9	10.34	0.030
99.75	+9.9	10.68	0.020
100.75	+10.9	10.91	0.040
103.84	+14.0	11.13	0.030
104.86	+15.1	11.15	0.030
105.87	+16.1	11.25	0.040
106.78	+17.0	11.18	0.030
107.83	+18.0	11.21	0.030
109.75	+19.9	11.15	0.020
	H band		
79.76	−10.0	9.83	0.060
80.85	−8.9	9.70	0.030
81.82	−8.0	9.67	0.040
82.79	−7.0	9.57	0.030
83.76	−6.0	9.57	0.040
84.72	−5.1	9.48	0.080
85.74	−4.1	9.54	0.070
86.77	−3.0	9.59	0.030
87.80	−2.0	9.58	0.040
90.78	+1.0	9.73	0.050
91.78	+2.0	9.75	0.050
92.79	+3.0	9.72	0.050
94.80	+5.0	9.68	0.050
95.80	+6.0	9.77	0.040
96.75	+6.9	9.77	0.040
97.77	+8.0	9.82	0.040
99.77	+10.0	9.80	0.050
100.76	+11.0	9.85	0.040
103.86	+14.1	9.79	0.040
104.87	+15.1	9.76	0.040
105.88	+16.1	9.82	0.050
106.78	+17.0	9.74	0.040
107.85	+18.1	9.71	0.030
109.76	+20.0	9.68	0.030
	K band		
79.76	−10.0	9.80	0.080
80.88	−8.9	9.53	0.060
81.85	−7.9	9.48	0.070
82.82	−7.0	9.40	0.050
83.77	−6.0	9.36	0.050
84.72	−5.1	9.27	0.100
85.75	−4.1	9.27	0.090
86.77	−3.0	9.25	0.040
87.80	−2.0	9.25	0.060
91.78	+2.0	9.35	0.070
92.79	+3.0	9.41	0.080
94.81	+5.0	9.41	0.070
95.81	+6.0	9.44	0.060
96.77	+7.0	9.45	0.060
97.79	+8.0	9.52	0.050
99.79	+10.0	9.48	0.060
100.77	+11.0	9.52	0.080
103.87	+14.1	9.56	0.070
104.87	+15.1	9.58	0.060
105.88	+16.1	9.54	0.060
106.78	+17.0	9.55	0.050
107.85	+18.1	9.58	0.050
109.77	+20.0	9.54	0.040

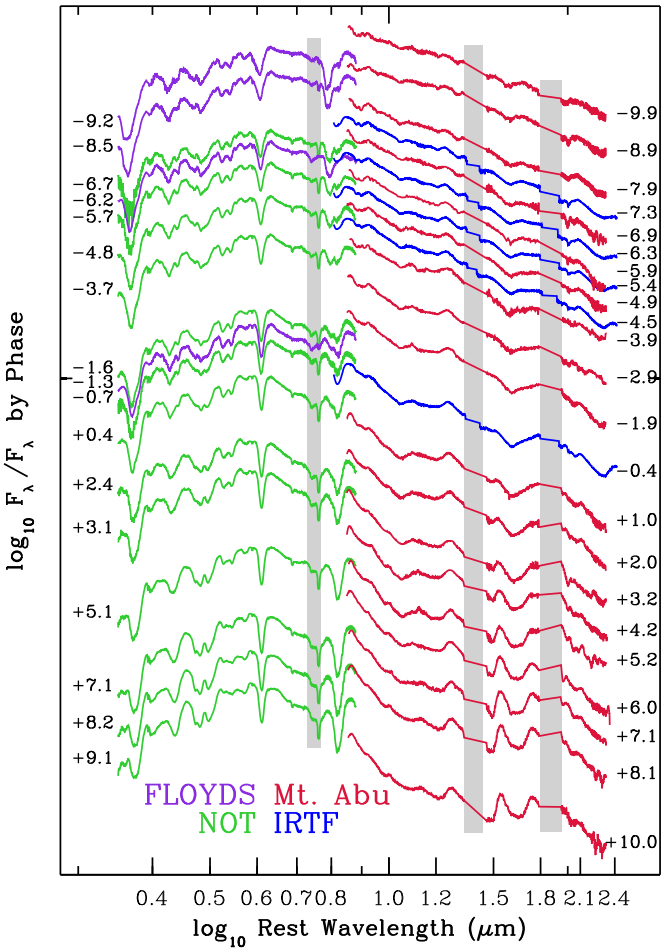

Figure 2. OIR spectra of SN 2014J from 0.32–2.4 μm obtained between −10d and +10d. The phases are marked at the red end for the NIR spectra and at the blue end for the optical spectra. The observatories are listed in colors that correspond to the colors of the spectra obtained at each facility. Vertical gray bars indicate regions of low atmospheric transmission.

photometry of SN 2014J; further details of the reduction process have been presented by Das et al. (2008).

The IRTF data were taken with SpeX (Rayner et al. 2003) in cross-dispersed mode and a 0.″3 slit, yielding a wavelength coverage of 0.8–2.5 μm, at $R = 2000$, divided over six orders. A0V stars were used as telluric standards. The data were reduced and calibrated using the publicly available Spextool software (Cushing et al. 2004), and corrections for telluric absorption

were performed using the IDL tool XTELLCOR developed by Vacca et al. (2003).

3. LIGHT CURVE PROPERTIES

We report some basic LC parameters, such as the time of maximum light and the decline rate in the *B* band, in order to provide context for our spectroscopic results. A full analysis of the SN 2014J LC is beyond the scope of the current work, and we note that a definitive analysis will require both difference imaging photometry (with template images constructed after the SN has faded) and detailed knowledge of the filter transmissions at every telescope where data were taken.

We use the LC fitting package SNooPy (SNe in Object-Oriented Python; Folatelli et al. 2010; Burns et al. 2011) with the *BVRIJH* photometry. The *BVRI* light curves are fit with the templates of Prieto et al. (2006), while the *JH* LCs are fit with the templates of Burns et al. (2011). Analyses of the LCs of SN 2014J by other groups indicate a total to selective extinction of $R_V \approx 1.4$ (Goobar et al. 2014; Amanullah et al. 2014), and so we adopt "calibration 4" within the SNooPY package, which corresponds to $R_V \approx 1.46$ (Folatelli et al. 2010). Note that since SNooPy incorporates a time-dependent correction for reddening, it is not necessary to do any additional corrections to the output LC decline parameter (i.e., Phillips et al. 1999), as this is automatically incorporated into the analysis (see Burns et al. 2011, for details).

The best fit SNooPy results have a maximum *B*-band magnitude of 11.68 ± 0.01 mag on $MJD = 56689.74 \pm 0.13$ (February 1.74 UT) with $\Delta m_{15} = 1.11 \pm 0.02$ mag. The $E(B-V)_{\rm host} = 1.23 \pm 0.06$ mag, and the implied distance modulus is $\mu + \log_{10}(H_0/72) = 27.85 \pm 0.09$ mag. We adopt the Dalcanton et al. (2009) TRGB distance modulus ($\mu = 27.64 \pm 0.1$ mag) and use $E(B-V)_{\rm MW} = 0.05$ with a standard $R_V = 3.1$ to derive $M_B = -19.19 \pm 0.10$ mag. Although this initial analysis does not take into account several possible sources of systematic uncertainty, these results are consistent with an average luminosity SN Ia, albeit in a dusty environment.

SNooPy simultaneously evaluates data from all of the filters and uses templates fit to the entire LC. Consequently, the SNooPy parameter Δm_{15} describes the LC shape, but it is not the same as the decline rate parameter $\Delta m_{15}(B)$ that is measured directly from the *B*-band LC. Burns et al. (2011) provide a conversion formula of $\Delta m_{15}(B) = 0.13 + 0.89 \times \Delta m_{15}$ to estimate the decline rate parameter from the SNooPy results. Using this formula, we find $\Delta m_{15}(B) = 1.118$ mag, which we round to 1.12 mag for discussion and comparison to other SNe Ia.

4. THE SPECTRA

Figure 2 displays 17 optical spectra and 23 NIR spectra that were obtained in the interval −10d to +10d. These spectra form a daily record of the rapidly changing absorption features as the effective photosphere recedes through the outer layers of the SN. Table 3 provides details of the spectroscopic observations.

4.1. Spectroscopic Comparisons to other SNe Ia

Spectral features are used to compare the physical properties of SNe Ia and for classification of SN types. While the LC parameters show that SN 2014J is a highly reddened but otherwise normal SN Ia, some of the spectroscopic parameters approach the limits for various definitions of "normal."

Table 4 lists velocity, pseudo equivalent width (pEW), and line depth for 10 features: Ca II λ3945 (H and K), Si II λ4130, Mg II λ4481, Fe II λ4900, S II λ5635, Si II λ5972, Si II λ6355, O I λ7773, Ca II λ8579, and Mg II λ1.0927. The measurements were taken from the optical spectrum obtained at +0.4d, except for Mg II λ1.0927, which was taken from the NIR spectrum obtained at −0.4d. Since we are focused on comparing values obtained near $t(B_{\rm max})$, all measurements and discussion refer to photospheric velocity features (PVFs). At earlier phases, high-velocity features (HVFs) are present for both strong Ca II blends but they have faded by $t(B_{\rm max})$.

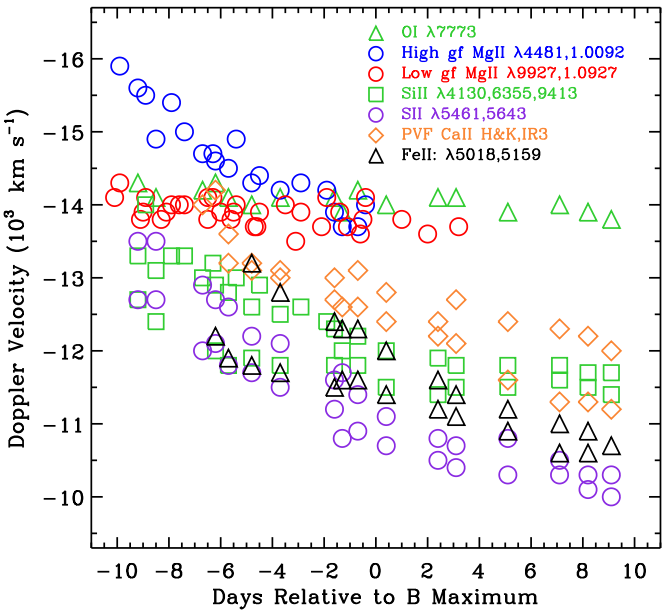

Figure 3. Velocity measurements for several lines plotted by phase. Mg II velocities before −3d form two groups that appear to be correlated with oscillator strength. The low *gf* Mg II lines (red) and O I remain essentially constant after −9d, while the high *gf* Mg II lines (blue) are about 2000 km s^{-1} faster at −10d. They decline quickly and reach the same velocity as other Mg II lines by about −4d. Si II velocities appear to establish a plateau at about +2d. S II and Fe II continue to decline. Velocity measurements are listed in Tables 5 and 6.

Three of the features (Mg II λ4481, Fe II λ4900, and S II λ5635) are broad absorption regions that include several blended lines. Regional boundaries for the pEW measurements are described by Garavini et al. (2007). The data are smoothed for measurement using a cubic spline interpolation in the region of each feature. The absorption minima, pEW, and line depths are measured after normalizing to a flat continuum.

The velocities of strong lines, the comparative velocities between lines and the rates of change for the velocities are among the most common spectral characteristics used to compare SN Ia. Figure 3 displays the measured velocities by phase for several lines that form optical or NIR features in the spectra of SN 2014J. The velocities for all phases are listed in Tables 5 and 6.

We compare measurements of SN 2014J with other SNe Ia using the tables and figures from several large samples of spectra (e.g., Benetti et al. 2005; Branch et al. 2006; Wang et al. 2009; Folatelli et al. 2010, 2012; Foley et al. 2011; Blondin et al. 2012; Silverman et al. 2012).

Wang et al. (2009) defined a simple and widely quoted sub-classification scheme for SNe Ia that separates them into normal velocity (NV) and HV classes. The discriminant is the velocity of the Si II λ6355 feature measured near $t(B_{\rm max})$ ($v_{\rm Si}$). The NV and HV classes are divided at 11,800 km s^{-1}, although some authors use 12,000 km s^{-1}.

Table 3
Log of Spectroscopic Observations

UT Date	MJD +56600	Phase wrt $t(B_{max})$[a]	Observatory/ Instrument	N Exp	I. Time (s)	Airmass SN 2014J	Telluric/Flux Standard	Airmass Standard
			NIR					
2014 Jan 22	79.86	−9.9	Mt Abu	4	480	1.42	SAO27682	1.15
2014 Jan 23	80.93	−8.9	Mt Abu	6	720	1.46	SAO27682	1.18
2014 Jan 24	81.91	−7.9	Mt Abu	6	720	1.44	SAO14667	1.51
2014 Jan 25	82.45	−7.3	IRTF/SpeX	10	720	1.58	HIP52478	1.31
2014 Jan 25	82.88	−6.9	Mt Abu	6	720	1.42	SAO14667	1.44
2014 Jan 26	83.46	−6.3	IRTF/SpeX	12	720	1.52	HIP52478	1.30
2014 Jan 26	83.91	−5.9	Mt Abu	4	720	1.45	SAO14667	1.44
2014 Jan 27	84.42	−5.4	IRTF/SpeX	12	960	1.64	HIP52478	1.43
2014 Jan 27	84.85	−4.9	Mt Abu	4	720	1.41	SAO14667	1.36
2014 Jan 28	85.30	−4.5	IRTF/SpeX	12	2000	2.45	HIP45590	2.25
2014 Jan 28	85.87	−3.9	Mt Abu	5	900	1.42	SAO14667	1.38
2014 Jan 29	86.88	−2.9	Mt Abu	6	900	1.42	SAO14667	1.39
2014 Jan 30	87.90	−1.9	Mt Abu	4	720	1.44	SAO14667	1.49
2014 Feb 1	89.39	−0.4	IRTF/SpeX	12	840	1.67	HIP52478	1.45
2014 Feb 2	90.77	+1.0	Mt Abu	6	720	1.47	SAO14667	1.35
2014 Feb 3	91.82	+2.0	Mt Abu	10	1200	1.42	SAO14667	1.37
2014 Feb 4	92.96	+3.2	Mt Abu	8	960	1.60	SAO14667	1.96
2014 Feb 5	93.96	+4.2	Mt Abu	6	1080	1.64	SAO14667	1.72
2014 Feb 6	94.95	+5.2	Mt Abu	10	1200	1.59	SAO14667	1.63
2014 Feb 7	95.78	+6.0	Mt Abu	10	1200	1.44	SAO14667	1.35
2014 Feb 8	96.93	+7.1	Mt Abu	10	1800	1.55	SAO14667	1.54
2014 Feb 9	97.92	+8.1	Mt Abu	8	960	1.54	SAO14667	1.58
2014 Feb 11	99.84	+10.0	Mt Abu	6	1080	1.42	SAO14667	1.45
			Optical[b]					
2014 Jan 23	80.62	−9.2	FTN/FLOYDS	1	600	1.72	...	...
2014 Jan 24	81.29	−8.5	FTN/FLOYDS	1	900	2.51	...	...
2014 Jan 26	83.13	−6.7	NOT/ALFOSC	3	180	1.32	...	...
2014 Jan 26	83.55	−6.2	FTN/FLOYDS	1	900	1.55	...	...
2014 Jan 27	84.12	−5.7	NOT/ALFOSC	3	180	1.32	...	...
2014 Jan 28	85.01	−4.8	NOT/ALFOSC	3	180	1.43	...	...
2014 Jan 29	86.12	−3.7	NOT/ALFOSC	3	180	1.32	...	...
2014 Jan 31	88.22	−1.6	NOT/ALFOSC	3	180	1.48	...	...
2014 Jan 31	88.49	−1.3	FTN/FLOYDS	1	900	1.52	...	...
2014 Feb 1	89.14	−0.7	NOT/ALFOSC	3	180	1.34	...	...
2014 Feb 2	90.21	+0.4	NOT/ALFOSC	3	180	1.47	...	...
2014 Feb 4	92.16	+2.4	NOT/ALFOSC	1	180	1.38	...	...
2014 Feb 4	92.93	+3.1	NOT/ALFOSC	1	180	1.62	...	...
2014 Feb 6	94.93	+5.1	NOT/ALFOSC	1	180	1.61	...	...
2014 Feb 8	96.91	+7.1	NOT/ALFOSC	3	180	1.66	...	...
2014 Feb 9	97.99	+8.2	NOT/ALFOSC	3	180	1.40	...	...
2014 Feb 10	98.93	+9.1	NOT/ALFOSC	3	180	1.57	...	...

Notes.
[a] MJD of $B_{max} = 56689.8$ (Feb 01.8).
[b] Instrumental sensitivity functions are very stable. Calibrations performed with previously observed standards.

To estimate v_{Si} at +0d, we fit a fourth order polynomial to the Si II λ6355 velocity data. At +0d, $v_{Si} = 12{,}000\,km\,s^{-1}$, which means that SN 2014J is an HV object, but not very far from the boundary with the NV group. The velocities of other Si II lines are similar although they are distorted by local influences. Si II λ4130 is 600–1000 km s^{-1} lower velocity than Si II λ6355 while Si II λ0.9413 has a velocity 900 km s^{-1} greater at −8.5d but only 400 km s^{-1} higher at −1.3. In comparison to other SNe Ia, the Fe II and S II velocities are HV, while O I is strongly in the HV category. Both Ca II H and K and the Ca II infrared triplet (IR3) velocities are NV but near the top of the range.

In addition to velocity, the relative sizes and shapes of absorption features are used to compare SNe Ia. Other subclasses are defined by combinations of spectral characteristics, including the Branch et al. (2006) subtypes: core normal (CN), broad line (BL), shallow silicon (SS), and cool (CL).

Where line profile parameters (depth, pEW, FWHM) are compared for large groups of SNe Ia, the resulting plots do not significantly separate the regions of NV and HV, CN and BL, and low-velocity gradient (LVG) and high-velocity gradient (HVG) objects. SS and CL objects are usually found in distinctly separate regions. SN 2014J fits into these blended regions of parameter space, so a subtype is not well defined. When most parameters are compared to Δm_{15}, a similar blending of subtypes occurs, but SN 2014J is always found in parameter space with HV, NV, CN, and BL objects. If, however, the parameter comparison clearly separates HV and NV objects or it separates the four Branch et al. (2006) groups into separate regions, then

Table 4
Measurements of Spectral Features at $t(B_{max})$

Ion + Wavelength	Velocity 10^3 km s^{-1}	pEW Å	Depth Normalized
Ca II 3945	−14,100	279	−1.34
Si II 4130	−11,500	20	−0.25
Mg II 4481	−13,700	93	−0.48
Fe II 4900	...	185	−0.51
S II 5635	−10,700	112	−0.45
Si II 5972	−11,300	12	−0.09
Si II 6355	−11,900	105	−0.65
O I 7773	−13,900	102	−0.30
Ca II 8579	−14,000	206	−0.58
Mg II 1.0927	−14,100	32	−0.20

SN 2014J is located in the HV or BL groups. Despite favoring these subtypes, the SN is seldom far from the boundaries with the NV or CN group.

The velocity gradient ($\dot{v}$) was defined by Benetti et al. (2005) as the average change per day of v_{Si} between two phases of observation. $\dot{v}$ is often calculated using the velocities at $t(B_{max})$ and +10d, but the time interval varies by publication based on the phases of the available data. In our sample, the latest phase for an optical spectrum is +9.1d. We fit a line to the data from −0.4d to +9.1d and find that $\dot{v}$ for +0d to +9.1d is 42 km s^{-1} day^{-1}, which is generally considered to be in the LVG group (Benetti et al. 2005). In cross references with other parameters, Blondin et al. (2012) places $\dot{v} = 44$ km s^{-1} day^{-1} near the middle of the CN group.

Foley et al. (2011) suggest including pre-maximum data by using the phase range of −6d to +10d. Fitting a line to the v_{Si} values for the interval −6.2d to +9.1d increases $\dot{v}$ to 74 km s^{-1} day^{-1}. Comparing this value to $\Delta m_{15}(B) = 1.12$ puts SN 2014J close the best-fit line for these parameters in the Foley et al. (2011) sample. We note that the pre-maximum portion of this range (−6.2d to +0d) has $\dot{v} = 134$ km s^{-1} day^{-1}. That value is well into the Benetti et al. (2005) HVG range. SN 2014J has a significant difference in the slope of the decline rate for Si II λ6355 velocities before and after $t(B_{max})$.

Equation (4) in Foley et al. (2011) estimates v_{Si} for a given time in the interval −6d to +10d and a given value of v_0.

$$v_{Si\,II}(t) = v_0(1 - 0.0322t) - 0.285t \quad (1)$$

(Note that this equation uses negative expansion velocities to indicate blueshifted features and the velocity units are 10^3 km s^{-1}.) Using $v_0 = -12.0$, the formula predicts $\dot{v} \approx 101$ km s^{-1} day^{-1}. This result is in reasonably good agreement with our pre-maximum measurements of v_{Si} in SN 2014J. After $t(B_{max})$, the measured velocities for SN 2014J decline more slowly than the formula estimates.

The pEW values for SN 2014J are always near the center of the range for $v_{Si} = 12{,}000$ km s^{-1}, but, where pEW for different lines are directly compared, the pEW for Si II λ6355 = 105 Å is in the BL sub-class. The position of SN 2014J on the plots is not far from CN objects for which pEW < 100 Å. The relatively low pEW (Si II λ5972) = 12 Å is associated with HV and BL objects, and for pEW (Si II λ4130), the CN and BL groups are mostly separate, with a small overlapping region that includes SN 2014J.

These comparisons demonstrate that SN 2014J is similar to a CN SN Ia with $v_0 \approx 12{,}000$ km s^{-1} and $\Delta m_{15}(B) \approx 1.12$ before $t(B_{max})$ and more like a BL SN Ia from +0d to +9.1d.

4.2. Carbon

Since the progenitor of an SN Ia is expected to be a carbon–oxygen white dwarf star, the detection of carbon would be evidence of unburned material from the progenitor. Absorption features from C II λλ6580, 7235 are frequently identified in spectra of normal SNe Ia more than 10 days before $t(B_{max})$, but they evolve rapidly and are usually undetectable after −10d (Thomas et al. 2011a; Parrent et al. 2011; Folatelli et al. 2012; Silverman & Filippenko 2012; Blondin et al. 2012).

Parrent et al. (2011) showed that C II λ6580 features appear to be ubiquitous in the early spectra of LVG SN Ia. However,

Table 5
Velocity Measurements of Absorption Features in Optical Spectra (10^3 km s^{-1})

Phase wrt $t(B_{max})$[a]	O I 7773 Å	Mg II 4481 Å	Mg II 9227 Å	Si II 4130 Å	Si II 6355 Å	S II 5463 Å	S II 5641 Å	Ca II 3945 μm	Ca II 8579 Å	Fe II 5018 Å	Fe II 5169 Å
−9.2	−14.3	−15.6	−13.3	−12.7	−13.3	−13.5	−12.7	pnm[b]	pnm[b]	...	...
−8.5	−14.1	−14.9	−13.2	−12.4	−13.1	−13.5	−12.7	pnm[b]	pnm[b]	...	...
−6.7	−14.2	−14.7	−13.5	...	−13.0	−12.9	−12.0	...	−14.0	...	...
−6.2	−14.3	−14.6	−13.3	−12.0	−12.9	−12.7	−12.1	−14.2	...	−12.2	...
−5.7	−14.1	−14.5	−13.3	−11.8	−12.8	−12.6	−11.8	−13.2	−13.6	−11.9	...
−4.8	−14.0	−14.3	−13.1	−11.9	−12.6	−12.2	−11.7	−13.1	−13.2	−11.8	−13.2
−3.7	−14.1	−14.2	−13.4	−11.8	−12.5	−12.1	−11.5	−13.0	−13.1	−11.7	−12.8
−1.6	−14.1	−13.9	−13.3	−11.8	−12.3	−11.6	−11.2	−13.0	−12.7	−11.5	−12.4
−1.3	−13.9	−13.7	−13.1	...	−12.0	−11.7	−10.8	−12.6	...	−11.6	−12.3
−0.7	−14.2	−13.7	−13.2	−11.8	−12.2	−11.4	−10.9	−13.1	−12.6	−11.6	−12.3
+0.4	−14.0	...	...	−11.5	−12.0	−10.9	−10.7	−12.8	−12.4	−11.4	−12.0
+2.4	−14.1	...	...	−11.4	−11.9	−10.7	−10.5	−12.4	−12.2	−11.2	−11.6
+3.1	−14.1	...	...	−11.5	−11.8	−10.8	−10.4	−12.7	−12.1	−11.1	−11.4
+5.1	−13.9	...	...	−11.5	−11.8	−10.8	−10.3	−12.4	−11.6	−10.9	−11.2
+7.1	−14.0	...	...	−11.6	−11.8	−10.5	−10.3	−12.3	−11.3	−10.6	−11.0
+8.2	−13.9	...	...	−11.5	−11.7	−10.3	−10.1	−12.2	−11.3	−10.6	−10.9
+9.1	−13.8	...	...	−11.4	−11.7	−10.3	−10.0	−12.0	−11.2	...	−10.7

Notes.
[a] MJD of B_{max} = 56689.8 (Feb 01.8).
[b] pnm = present, not measured. An indication that the feature is present but lacks a distinct minimum.

Table 6
Velocity Measurements of Absorption Features in Near-Infrared Spectra (10^3 km s^{-1})

Phase wrt $t(B_{max})$[a]	Mg II 4481 Å[b]	Mg II 9227 Å[b]	Mg II 0.9227 μm	Mg II 1.0092 μm	Mg II 1.0927 μm	Si II 0.9413 μm
−9.2	−15.6	−13.3	−13.5	−15.9	−14.3	...
−8.5	−14.9	−13.2	−13.2	−15.5	−14.1	−14.0
−6.7	−14.7	−13.5	−13.3	−15.4	−14.0	−13.3
−6.2	−14.6	−13.3	−13.4	−15.0	−14.0	−13.3
−5.7	−14.5	−13.3	−13.2	−14.7	−14.1	−13.2
−4.8	−14.3	−13.1	−13.2	−14.9	−14.0	−13.0
−3.7	−14.2	−13.4	−13.1	−14.4	−13.9	−12.9
−1.6	−13.9	−13.3	−12.9	−14.3	−13.9	−12.6
−1.3	−13.7	−13.1	−13.1	−14.2	−14.1	−12.4
−0.7	−13.7	−13.2	−13.0	−14.0	−14.1	...
+0.4	...	...	...	...	−13.8	...
+2.4	...	...	...	...	−13.6	...
+3.1	...	...	...	...	−13.7	...

Notes.
[a] MJD of B_{max} = 56689.8 (Feb 01.8).
[b] Lines measured in optical spectra are included here to facilitate comparison of Mg II velocities.

Zheng et al. (2014) and Goobar et al. (2014) reported no carbon detections in the optical spectra of SN 2014J. Two factors contribute to this discrepancy. First, the earliest spectra were obtained only 10 days before $t(B_{max})$, at a phase when C II is already difficult to detect in normal SNe Ia. Second, many strong absorption features from diffuse interstellar bands (DIBs) appear in the optical spectra of SN 2014J. Two of these DIB are perfectly positioned to obscure evidence for C II λλ6580, 7235. In the NIR, C II lines are not good candidates for carbon detection. They are significantly weaker than optical lines due to much higher excitation potentials.

This is not, however, the last word on carbon in SN 2014J because C I lines may be detectable in the NIR. Marion et al. (2006) used non-detections of C I in a small sample of NIR spectra to place constraints on the carbon abundance of SNe Ia. Hsiao et al. (2013) showed that distortions in the blue wings of the Mg II λ1.0927 features can be fit by synthetic spectra that include C I λ1.0693, and they suggested that C I may be present in most SNe Ia.

Figure 4 shows evidence for the presence of C I in NIR spectra. The vertical dashed line shows where profiles of Mg II λ1.0927 are flattened on the blue side from −8d to +2d. This location is consistent with C I λ1.0693. The dotted line superimposed on the −0.4d spectrum shows the approximate location of the line profile if C I were absent. The Mg II features from −7.9d to +2.0d show similar evidence of flattening in this region.

This figure also demonstrates that after about +3d, the weakening contributions from C I and Mg II become indistinguishable as part of a blended feature that includes increasing contributions from Fe II λλ0.9995, 1.0500, 1.0863. The spectra in this figure have been smoothed with a Fourier Transform technique (Marion et al. 2009). Smoothing is necessary because some of the spectra have high noise levels that make it difficult to see the broader SN features when viewing the data at this scale.

We also use synthetic spectra from SYNAPPS (Thomas et al. 2011b) models to investigate how C I λ1.0693 may influence the Mg II λ1.0927 features. Figure 5 shows the −0.4d spectrum of SN 2014J plotted as a black solid line. This spectrum is the closest to $t(B_{max})$ and it is the same spectrum shown in Figure 4.

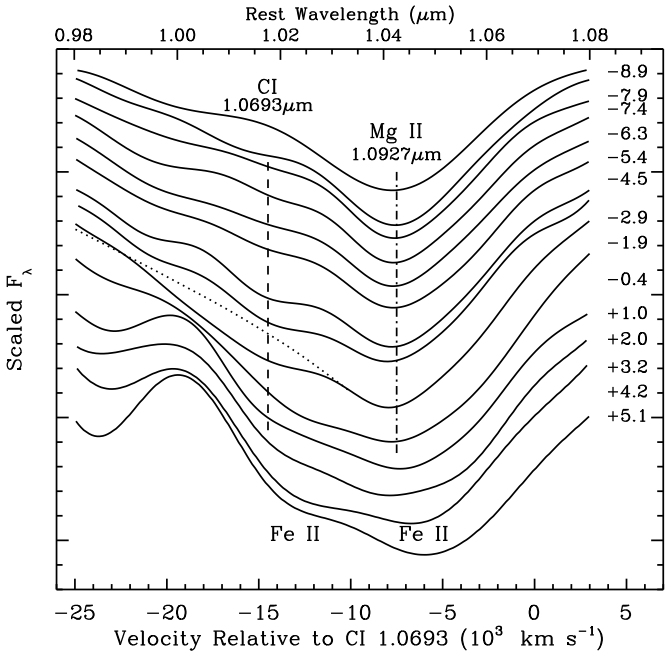

Figure 4. NIR spectra from −9d to +5d are normalized to a level continuum over the region 0.98–1.08 μm and zoomed in on the blueshifted Mg II λ1.0927 feature. The velocity space on the bottom axis is calibrated to the C I λ1.0693 line. C I flattens the blue wing of the Mg II feature from −7.4d to +3.2d. The spectrum closest to $t(B_{max})$ (−0.4d) is compared to models in Figure 5 and discussed in the text. The dotted line shows the approximate shape of the line profile predicted by the model when C I is absent. The dashed line corresponds to the absorption minimum of C I in models that fit the data well and the dash–dotted line marks the absorption minima for Mg II.

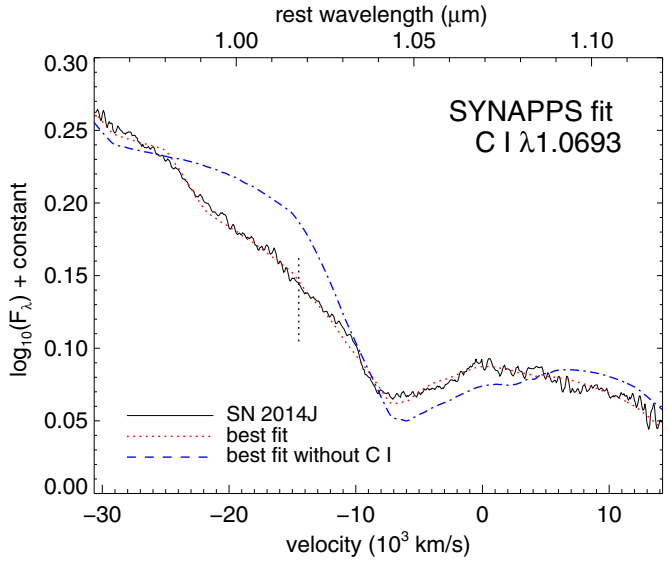

Figure 5. SYNAPPS models show that C I λ1.0693 is required to match the line profile of the Mg II λ1.0927 feature. The solid black line is the −0.4d spectrum of SN 2014J. These are the same data found in Figure 4, but plotted here without smoothing. The spectrum displayed as a red dotted line is a good fit to the data. It was produced by a model that includes multiple ions plus C I. The spectrum plotted as a blue dot–dashed line is a poor fit to the absorption feature. It was produced by removing C I from the model. The short dotted line marks the location of the absorption minimum for C I in the model.

The high signal-to-noise IRTF spectrum is shown here without smoothing.

The same modeling parameters are used for all ions to calculate the synthetic spectra. The red dotted line in the figure is a SYNAPPS model spectrum that includes all ions that have

been identified in the spectra of SN 2014J, plus C I. The dotted line is a very good fit to the real data.

Removing C I from the ions available to SYNAPPS produces the spectrum plotted with dashes and dots. This model shows the Mg II line profile without the contribution of C I and the result is a poor fit to the data. The dotted line added to Figure 4 approximates the position of the dash-dotted line in this figure.

The short, vertical dotted line at 14,500 km s^{-1} in Figure 5 represents the approximate location of the absorption minimum for C I in the model. That velocity is lower than predicted for the carbon region by most explosion models and it is higher than usually found for C II λ6580 (Parrent et al. 2011).

Another possibility is that a separated high-velocity Mg II line forming region is responsible for the observed distortions. Marion et al. (2013) shows that most HVFsfor intermediate mass elements (IMEs) have absorption minima of 20–22,000 km s^{-1}. The velocity difference from C I λ1.0693 to Mg II λ1.0927 is about 6500 so the velocity indicated by the dashed vertical line in Figure 4 is reasonable for the HVFs of Mg II. However, Marion et al. (2013) also showed that the HVFs of IMEs were only detected in spectra obtained before −10d. There is no evidence for HVFs of the Si II λ6355 line at any phase. Figure 4 shows that the earliest possible detection of HVFs is at −7.9d. That timing is consistent with C II recombining to form C I and it is very different than any previous detections of HVFs for IMEs. Consequently, we find it improbable that the HVFs of Mg II λ1.0927 make any contribution to the absorption or flattening that we attribute to C I.

The SYNAPPS model spectrum is a good fit to the data at −0.4d, and the data quality are high. We find it likely that C I λ1.0693 is responsible for the flattening of the blue wing of the Mg II λ1.0927 feature. These results suggest that carbon may be present in the chemical structure of SN 2014J. The relative timing of the C I detections is consistent with ionized carbon beginning to recombine at about −9d as the carbon-rich layer expands and cools. The weakness of the carbon features suggest that nearly all of the initial white dwarf material along the line-of-sight to the SN was burned during the explosion.

4.3. Magnesium

Magnesium lines have low excitation potentials so that Mg in normal SNe Ia remains ionized until it is no longer detected, which usually occurs a few days after $t(B_{\max})$ in SNe Ia (Marion et al. 2009). Several Mg II lines are detectable in NIR spectra, but we confine this study to one optical and three NIR lines that are strong and relatively unblended in the early spectra.

Mg II λ1.0927 is the easiest Mg II line to measure because it forms a strong absorption, it is relatively unblended, and it is easy to estimate the continuum location through this region. The measured velocity of this line is −14,300 km s^{-1} at −10d, and it subsequently remains −14,000 km s^{-1} through +3d which is the last day of that Mg II is clearly detected. After +3d, this feature is blended with Fe II lines that make it impossible to distinguish the Mg II feature. These velocity measurements are consistent with the suggestion by Hsiao et al. (2013) that Mg II λ1.0927 velocities will be constant in normal SNe Ia after a brief period of decline at very early times.

We measure Mg II λ0.9227 in both optical and NIR spectra and the velocities agree within 300 km s^{-1}. This is a strong line, but the blue side of the profile is compressed and the absorption minimum is pushed to the red by the enormous P Cygni emission from the Ca II infrared triplet. The distortion is well known and Marion et al. (2009) suggested that measured Mg II λ0.9227 velocities should be increased by 500–1000 km s^{-1} for comparison to other line velocities. Tables 5 and 6 have the measured velocities for Mg II λ0.9227, while Figure 3 plots the measured values plus 500 km s^{-1}.

Absorption features from other Mg II lines are obscured and unmeasurable. Mg IIλ7890 is blended with O I λ7773 and a strong DIB sits at the location of a 14,000 km s^{-1} feature from this line. Potential features from Mg II λ1.8613 are in a region of high opacity between the *H* and *K* bands. Mg II λ0.8228 is obscured by the huge feature from the Ca II infrared triplet (IR3).

Figure 3 shows that the −10d velocities for Mg II λ4481 and λ1.0092 (blue circles) are about 2000 km s^{-1} higher than Mg II λλ0.9227, 1.0927 (red circles). The velocity difference diminishes rapidly, and by about −4d all Mg II velocities are found in a narrow range near −14,000 km s^{-1}. The different Mg II velocities in the early spectra can be explained by differences in the optical depths of the lines. The Mg II lines with higher initial velocities are also the lines with the highest oscillator strengths. The gf value is a measure of the oscillator strength, or interaction cross-section, for each line. Mg II λ4481 and λ1.0092 have relatively high oscillator strengths with log $gf = 0.74$ and 1.02, respectively, while Mg II λλ0.9227, 1.0927 have log $gf = 0.24$ and 0.02.

Jeffery & Branch (1990) showed that an increase in line optical depths will shift the minima of observed line profiles to higher velocities. This happens because the higher optical depth causes more of the observed flux to come from scattering rather than directly from the photosphere. Scattering takes place at larger radii, and thus higher velocities, and the observed velocity increases even though the location of the line forming region does not change.

When abundance is spatially constant, Sobolev optical depth is proportional to the effective line strength. Both oscillator strength and excitation potential contribute to the effective strength of each line, but the relative influence of oscillator strength is temperature-dependent. The optical depth for lines with higher gf values is more responsive to temperature changes than it is for lines with low gf values. Consequently, the relative optical depths can change with temperature for two lines from the same ion but with different gf values.

The observed behavior of Mg II velocities in the early spectra of SN 2014J is consistent with the time-dependent Sobolev optical depths of these lines (Jeffery & Branch 1990). The high gf lines have greater optical depths at −10d, so they form absorption minima at larger radii and produce higher observed velocities than the low gf lines. As the SN expands, the number density and the excitation temperature of the Mg line forming region decrease, causing the optical depths to decrease for all Mg features. The reduced optical depths move the absorption minima of the high gf features to lower velocities, while the low gf features remain at a constant velocity determined by the inner edge of the Mg line forming region.

The velocities of other ions are near Mg II velocities for the first few days of our observations, but they decline continuously through +10d while O I and Mg II velocities remain constant. This happens because the O I and Mg II line forming region is fixed in radial and velocity space. It becomes "detached" as the velocity of the effective photosphere recedes with time, creating a physical separation in radial space (Jeffery & Branch 1990).

4.4. Other Spectral Features

Absorption features from O I λ7773 remain near −14,000 km s^{-1} for the entire period covered by our sample.

O I and Mg II have similar velocities at all phases when Mg II is detected.

Si II λ6355 velocities at −10d and −9d are about 1000 km s^{-1} lower than those reported by Goobar et al. (2014), but we agree closely from −8d to +2d which is the latest measurement in their sample. Velocity measurements of NIR Si II λ0.9413 are consistent with the optical Si II λ6355. An HVF may be present for Si II λ6355 at −10d and −9d but a strong absorption from Na I distorts this region and makes confirmation difficult for a separate Si II λ6355 component.

HVFs of Ca II are observed for both the H and K and infrared triplet (IR3) blends at velocities of about −26,000 km s^{-1} at −10d and ≈−20,000 km s^{-1} at $t(B_{\rm max})$. HVFs are detected from −10d to +0d in both the NIR spectra that cover Ca II IR3, and the optical spectra that cover both Ca II H and K and IR3. At −10d and −9d, we resolve separate components for the two strongest lines in the IR3 blend (0.8542 and 0.8662 μm). HVF velocities are not included in Figure 3 to avoid extending the vertical axis which would make it more difficult to see the PVF velocities.

PVFs of Ca II are present in the earliest spectra in our sample where they clearly form depressions in the red side of the absorptions formed by the HVFs. The first distinct minimum is for Ca II H and K PVF at −14,200 km s^{-1} on −6.2d. The PVF features become stronger through the time covered by our sample and the velocities slowly decline.

Ca and Fe detections at these early phases are likely to be from atoms that were part of the pre-explosion atmosphere. Fe II features are first clearly identified at −6d with Fe II λ5018 having a velocity of −12,200 km s^{-1}. From −6d to +9d, Fe II velocities are comparable to Si II. Figure 3 shows that Fe II velocities continue to decline after $t(B_{\rm max})$ when Si II and Ca II velocities have established minima.

Pre-maximum absorptions in the H band are dominated by Mg II λ1.6787 and then by a blend with Si II λ1.6930. Figure 6 shows that the post-maximum H-band features of SN 2014J follow the sequence first noted by Kirshner et al. (1973) and explained by Wheeler et al. (1998). Soon after $t(B_{\rm max})$, pseudo emission begins to create the large bumps observed at 1.54 and 1.75 μm. Line-blanketing from Fe-group lines increases the opacity at these wavelengths so that the effective photospheres are formed at radii well above the continuum and the observed flux increases.

H-band photometry of SNe Ia has been identified both theoretically (Kasen 2006) and observationally (Krisciunas et al. 2004, 2007; Wood-Vasey et al. 2008; Mandel et al. 2009, 2011) as having the least intrinsic scatter among the usual filter sets. One of the most important uses of post-maximum NIR spectra is to gain understanding of and to quantify the behavior of these large features in order to produce reliable NIR k corrections. The abrupt flux changes over a short wavelength range can significantly affect observed brightness in a particular filter, as wavelength changes due to redshift move the H-band features.

The H-band break ratio ($R = f1/f2$) was defined by (Hsiao et al. 2013) as the difference between the flux level just to the red of 1.5 μm and the flux level just blueward of 1.5 μm. The locations of $f1$ and $f2$ are marked in Figure 6 for the +10d spectrum. We measure R in the nine NIR spectra obtained between +1d and +10d, and the values are 0.2, 0.3, 0.6, 1.0, 1.6, 2.1, 2.9, 3.5, and 4.1. Figure 10 from (Hsiao et al. 2013) displays measurements of R by phase for several SNe Ia. The R values of SN 2014J are slightly higher at each phase than R values for the other SN Ia. The rate of increase is parallel to the slope of the combined measurements for the other SNe Ia. $R = 4.1$ at +10d is comparable to the +12d measurements of $R = 3.9$ for SN 1999ee and $R = 4.0$ for SN 2011fe. More NIR spectral sequences are required to fill in the parameter space for the H-band break ratio compared to Δm_{15} and other observables, but these measurements show that.

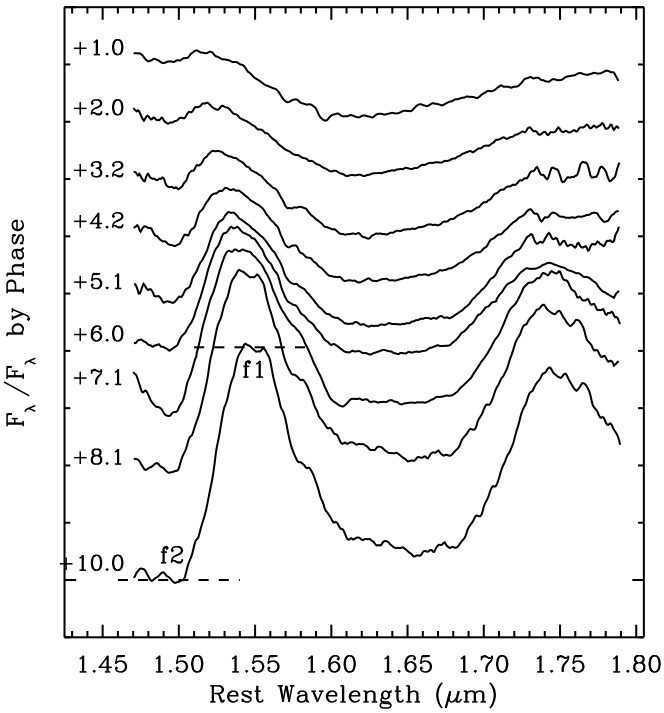

Figure 6. H-band features in SN 2014J during the first 10 days after $t(B_{\rm max})$. The prominent features centered at about 1.54 and 1.75 μm are formed by pseudo emission due to line-blanketing of Fe-group lines. The short dashed lines mark the flux levels used to measure the H-band break, $R = f1/f2$. The evolution of these features is important to NIR k corrections for SNe Ia.

4.5. Comparison to Model Predictions

During the phases covered by the spectra in our sample, SNe Ia have a well defined photosphere that is receding in velocity space through the outer layers of the atmosphere. A sequence of spectra can identify the chemical structure of the atmosphere in radial space. Figure 3 reveals that SN 2014J has a layered composition with little or no mixing.

Magnesium and oxygen are produced by carbon burning in regions where the densities and temperatures are high enough to burn carbon, but low enough to prevent further burning. These observations identify a O- and Mg-rich layer located in the outermost part of the ejecta ($\geqslant$14,000 km s^{-1}). The presence of a distinct minimum velocity indicates a lower limit for the line forming region in radial space.

Si and S are IMEs that are found together in a velocity region below O and Mg. The velocities for Si and S decline throughout our period of observation, and there is no evidence for a minimum velocity of the IME layer by our final phase of optical spectra at +9d.

The Ca and Fe observed at these high velocities is likely to have been present in the atmosphere before the explosion. There is no evidence for large-scale mixing of freshly synthesized Ca or Fe into the physical region defined by velocities greater than 10,000 km s^{-1} along the line of sight. These are strong lines that produce detectable absorptions at very low abundances.

The observed features are formed near the photosphere and the velocities follow the declining photospheric velocity until the atmosphere becomes sufficiently transparent to expose material close to the core.

Radial stratification is evidence for detonation-driven burning that moved out in radial space through material with a monotonically decreasing density gradient. That result is consistent with delayed detonation (DDT) explosion models in which mixing only occurs during the subsonic deflagration phase and remains near the center of the progenitor (Höflich et al. 2002). Energy from the deflagration expands the progenitor and reduces the density toward the surface. A subsequent detonation produces the structure that we have observed in the outer layers of SN 2014J.

5. SUMMARY AND CONCLUSIONS

SN 2014J is a very nearby supernova that we were able to observe in considerable detail. Despite the fact that M82 has a well-determined distance, the extinction is large, so unlike SN 2011fe, this will not be a particularly useful case for anchoring the extragalactic distance scale.

We present optical and NIR spectra and LCs, with densely sampled data obtained during the first 40 days after discovery. We acknowledge uncertainties in the photometric measurements due to the high degree of reddening that will not be resolved until galaxy template images are available.

SNooPy is used to fit the $BVRIJH$ LCs. With $R_V = 1.46$, the SNooPy results are $A_V = 1.80$, $E(B-V)_{\rm host} = 1.23 \pm 0.01$ mag, $m_B = 11.68 \pm 0.01$, $t(B_{\rm max}) =$ February 1.74 UT ± 0.13 days, and $\Delta m_{15} = 1.11 \pm 0.02$ mag. We use $\mu = 27.64$ mag, $E(B-V)_{MW} = 0.05$, and R_V=3.1 to derive $M_B = -19.19 \pm 0.10$ mag. We convert the SNooPy parameter Δm_{15} to $\Delta m_{15}(B) = 1.12$ mag.

Spectroscopic parameters of SN 2014J are compared to other SNe Ia and most of the measurements fit into parameter spaces that are defined as normal for SNe Ia. The exceptions are not far outside the limits of normal, for example, $pv_{\rm Si} = 13{,}900$ km s^{-1} is barely into the Wang et al. (2009) HV group and pEW (Si II λ6355) = 105 Å is just into the Branch et al. (2006) BL group. Measurements of the H-band break ratio in SN 2014J show that the post-maximum development of prominent H-band features is consistent with normal SNe Ia.

Due to the relatively late discovery of SN 2014J and the presence of numerous DIBs in the optical spectra, it is difficult to prove or disprove the presence of carbon features in the optical spectra. We use NIR and model spectra to show evidence for the presence of C I λ1.0693. The implied velocity for C I is coincident with O I and Mg II velocities. We conclude that carbon is very likely to be present in SN 2014J.

Velocity measurements show that two Mg II lines exhibit higher velocities in the earliest spectra. We explore the relationships between the oscillator strengths of individual lines, the Sobolev optical depths, and the observed velocities of the features. We conclude that the higher initial velocities are due to increased optical depths that result from higher oscillator strengths of those lines.

The observations show that SN 2014J has a layered structure with no large scale mixing at velocities greater than 10,000 km s^{-1}. Products of carbon burning, O I, and Mg II, have the highest velocities and their line forming region has a distinct minimum at about 14,000 km s^{-1}. IMEs, Si II and S II, are located between 10,000 km s^{-1} and 14,000 km s^{-1}, but our observations end at +9d, before a velocity minimum is detected for this layer. A radial stratification of material with the lightest elements on the outside is consistent with detonation burning in a progenitor with a radial density gradient, as predicted by DDT explosion models.

G.H.M. and D.J.S. are visiting Astronomers at the Infrared Telescope Facility, which is operated by the University of Hawaii under Cooperative Agreement No. NNX-08AE38A with the National Aeronautics and Space Administration. We thank A. Tokunaga, D. Griep, E. Volquardsen, B. Cabreira, and J. Rayner at the IRTF for supporting ToO observations. We also acknowledge P. Donati, S. Geier, F. Saturni, G. Nowak, and A. Finoguenov for cooperating with NOT ToO observations. The NOT is operated by the Nordic Optical Telescope Scientific Association at the Observatorio del Roque de los Muchachos, La Palma, Spain, of the Instituto de Astrosica de Canarias. Research at the Physical Research Laboratory is funded by the Department of Space, Government of India.

J.V. is supported by the Hungarian OTKA Grant NN-107637. The UT supernova group is supported by NSF grant AST-1109801. J.M.S. is also supported by an NSF Astronomy and Astrophysics Postdoctoral Fellowship under award AST-1302771. J.J.B. gratefully acknowledges the support of NSF grant AST-1151462. R.P.K. is supported by NSF grant AST-1211196 to the Harvard College Observatory. Additional support comes from the program GO-12540, provided by NASA through a grant from the Space Telescope Science Institute, which is operated by the Association of Universities for Research in Astronomy, Inc., under NASA contract NAS5-26555. R.A. acknowledges support from the Swedish Research Council and the Swedish National Space Board. M.D.S. acknowledges generous support provided by the Danish Agency for Science and Technology and Innovation realized through a Sapere Aude Level 2 grant.

Facilities: IRTF (SpeX), NOT, LCOGT

REFERENCES

Amanullah, R., Goobar, A., Johansson, J., et al. 2014, ApJL, 788, L21
Banerjee, D. P. K., & Ashok, N. M. 2012, BASI, 40, 243
Benetti, S., Cappellaro, E., Mazzali, P. A., et al. 2005, ApJ, 623, 1011
Blondin, S., Matheson, T., Kirshner, R. P., et al. 2012, AJ, 143, 126
Boldt, L., Stritzinger, M., Burns, C., et al. 2014, PASP, 126, 324
Branch, D., Dang, L. C., Hall, N., et al. 2006, PASP, 118, 560
Brown, T. M., Baliber, N., Bianco, F. B., et al. 2013, PASP, 125, 1031
Burns, C. R., Stritzinger, M., Phillips, M. M., et al. 2011, AJ, 141, 19
Childress, M. J., Scalzo, R. A., Sim, S. A., et al. 2013, ApJ, 770, 29
Chomiuk, L. 2013, PASA, 30, 46
Churazov, E., Sunyaev, R., Isern, J., et al. 2014, Natur, 512, 406
Cushing, M. C., Vacca, W. D., & Rayner, J. T. 2004, PASP, 116, 362
Dalcanton, J. J., Williams, B. F., Seth, A. C., et al. 2009, ApJS, 183, 67
Das, R. K., Banerjee, D. P. K., Ashok, N. M., & Chesneau, O. 2008, MNRAS, 391, 1874
Folatelli, G., Phillips, M. M., Burns, C. R., et al. 2010, AJ, 139, 120
Folatelli, G., Phillips, M. M., Morrell, N., et al. 2012, ApJ, 745, 74
Foley, R. J., Challis, P. J., Filippenko, A. V., et al. 2012, ApJ, 744, 38
Foley, R. J., Sanders, N. E., & Kirshner, R. P. 2011, ApJ, 742, 89
Garavini, G., Folatelli, G., Nobili, S., et al. 2007, A&A, 470, 411
Goobar, A., Johansson, J., Amanullah, R., et al. 2014, ApJL, 784, L12
Höflich, P., Gerardy, C. L., Fesen, R. A., & Sakai, S. 2002, ApJ, 568, 791
Hsiao, E. Y., Marion, G. H., Phillips, M. M., et al. 2013, ApJ, 766, 72
Jeffery, D. J., & Branch, D. 1990, in Supernovae, Jerusalem Winter School for Theoretical Physics, ed. J. C. Wheeler, T. Piran, & S. Weinberg (Singapore: World Scientific), 149
Jha, S., Garnavich, P. M., Kirshner, R. P., et al. 1999, ApJS, 125, 73
Kasen, D. 2006, ApJ, 649, 939
Kasen, D. 2013, Natur, 502, 310
Kelly, P. L., Fox, O. D., Filippenko, A. V., et al. 2014, ApJ, 790, 3

Kirshner, R. P., Willner, S. P., Becklin, E. E., Neugebauer, G., & Oke, J. B. 1973, ApJL, 180, L97
Krisciunas, K., Garnavich, P. M., Stanishev, V., et al. 2007, AJ, 133, 58
Krisciunas, K., Phillips, M. M., & Suntzeff, N. B. 2004, ApJL, 602, L81
Mandel, K. S., Narayan, G., & Kirshner, R. P. 2011, ApJ, 731, 120
Mandel, K. S., Wood-Vasey, W. M., Friedman, A. S., & Kirshner, R. P. 2009, ApJ, 704, 629
Margutti, R., Parrent, J., Kamble, A., et al. 2014, ApJ, 790, 52
Marion, G. H., Höflich, P., Gerardy, C. L., et al. 2009, AJ, 138, 727
Marion, G. H., Höflich, P., Wheeler, J. C., et al. 2006, ApJ, 645, 1392
Marion, G. H., Vinko, J., Wheeler, J. C., et al. 2013, ApJ, 777, 40
Milne, P. A., Brown, P. J., Roming, P. W. A., Bufano, F., & Gehrels, N. 2013, ApJ, 779, 23
Nielsen, M. T. B., Gilfanov, M., Bogdan, A., Woods, T. E., & Nelemans, G. 2014, MNRAS, 442, 3400
Nugent, P. E., Sullivan, M., Cenko, S. B., et al. 2011, Natur, 480, 344
Parrent, J. T., Thomas, R. C., Fesen, R. A., et al. 2011, ApJ, 732, 30
Perlmutter, S., Aldering, G., Goldhaber, G., et al. 1999, ApJ, 517, 565
Phillips, M. M., Lira, P., Suntzeff, N. B., et al. 1999, AJ, 118, 1766
Prieto, J. L., Rest, A., & Suntzeff, N. B. 2006, ApJ, 647, 501
Rayner, J. T., Toomey, D. W., Onaka, P. M., et al. 2003, PASP, 115, 362
Riess, A. G., Filippenko, A. V., Challis, P., et al. 1998, AJ, 116, 1009
Schlafly, E. F., & Finkbeiner, D. P. 2011, ApJ, 737, 103
Schlegel, D. J., Finkbeiner, D. P., & Davis, M. 1998, ApJ, 500, 525
Silverman, J. M., & Filippenko, A. V. 2012, MNRAS, 425, 1917
Silverman, J. M., Ganeshalingam, M., Cenko, S. B., et al. 2012, ApJL, 756, L7
Suntzeff, N. B., Phillips, M. M., Covarrubias, R., et al. 1999, AJ, 117, 1175
The, L.-S., & Burrows, A. 2014, ApJ, 786, 141
Thomas, R. C., Aldering, G., Antilogus, P., et al. 2011a, ApJ, 743, 27
Thomas, R. C., Nugent, P. E., & Meza, J. C. 2011b, PASP, 123, 237
Vacca, W. D., Cushing, M. C., & Rayner, J. T. 2003, PASP, 115, 389
Valenti, S., Sand, D., Pastorello, A., et al. 2014, MNRAS, 438, L101
Wang, X., Li, W., Filippenko, A. V., et al. 2009, ApJ, 697, 380
Wheeler, J. C., Hoeflich, P., Harkness, R. P., & Spyromilio, J. 1998, ApJ, 496, 908
Wood-Vasey, W. M., Friedman, A. S., Bloom, J. S., et al. 2008, ApJ, 689, 377
Yaron, O., & Gal-Yam, A. 2012, PASP, 124, 668
Zheng, W., Shivvers, I., Filippenko, A. V., et al. 2014, ApJL, 783, L24
Zheng, W., Silverman, J. M., Filippenko, A. V., et al. 2013, ApJL, 778, L15